POLITECNICO DI TORINO
Repository ISTITUZIONALE

Back-diffusion of hydroxide ions governs failure mechanisms in asymmetric seawater electrolyzers

Original
Back-diffusion of hydroxide ions governs failure mechanisms in asymmetric seawater electrolyzers / Gardiol, P., Etzi, M., Sacco, A., Gho, C.I., Sassone, D.. - In: JOURNAL OF POWER SOURCES. - ISSN 0378-7753. - 690:(2026). [10.1016/j.jpowsour.2026.240833]

Availability:
This version is available at: 11583/3013092 since: 2026-07-14T08:38:22Z

Publisher:
Elsevier

Published
DOI:10.1016/j.jpowsour.2026.240833

Terms of use:

This article is made available under terms and conditions as specified in the corresponding bibliographic description in the repository

Publisher copyright

(Article begins on next page)

15 July 2026

Journal of Power Sources 690 (2026) 240833

Contents lists available at ScienceDirect

Journal of Power Sources

journal homepage: www.elsevier.com/locate/jpowsour

Back-diffusion of hydroxide ions governs failure mechanisms in asymmetric seawater electrolyzers

Paolo Gardiol [a,b], Marco Etzi [a], Adriano Sacco [a], Cecilia Irene Gho [a], Daniele Sassone [a,*]

[a] Center for Sustainable Future Technologies, Istituto Italiano di Tecnologia, Via Livorno 60, Torino, 10144, Italy
[b] Department of Electronic and Telecommunication, Politecnico di Torino, C.so Duca degli Abruzzi 24, Turin, 10129, Italy

HIGHLIGHTS

- OH^- diffuses from anolyte to seawater even without applied bias.
- Membrane properties dominate OH^- crossover over catalyst choice.
- Back-diffusion persists under current, causing delayed cathode failure.
- Findings suggest full-SWE as a more stable long-term solution.

ARTICLE INFO

Keywords:
Seawater
Back-diffusion
Half seawater electrolyzer
Anion exchange membrane
Basification

ABSTRACT

Seawater (SW) is an attractive alternative to freshwater for electrolysis due to its abundance, yet its direct use is hindered by competing chlorine evolution and cathodic precipitation failure. Half-seawater electrolyzers (half-SWE) have been proposed to partially mitigate these issues by coupling an alkaline anolyte with SW catholyte. In this work, we demonstrate how OH^- spontaneously diffuses from the anolyte into the SW even in the absence of applied bias. This transport persists under operating conditions, progressively increasing catholyte pH and triggering precipitation of insoluble hydroxides. Through systematic experiments across different membranes, thicknesses, and electrode configurations, we show that OH^- crossover is primarily governed by membrane properties rather than catalysts selection. While applied current partially counteracts back-diffusion, it does not suppress it, leading to delayed but unavoidable cathode failure. To quantitatively assess ion transport, we introduce an electron-transfer-based methodology, which decouples OH^- migration from parasitic reactions. This approach enables direct evaluation of OH^- transport efficiency, revealing intrinsic limitations below 80% due to concurrent back-diffusion and interfacial accumulation. These findings establish OH^- crossover as a fundamental constraint in half-SWE systems and highlight the need for design strategies that minimize pH gradients, pointing toward full-SWE as a more viable pathway for stable operation.

1. Introduction

Hydrogen is increasingly regarded as a central pillar in the decarbonization of energy systems, owing to its high energy density and its versatility in end-use applications [1,2]. Conventional water electrolysis (alkaline or acidic) already offers commercial maturity [3], but it depends on high-purity water feedstock [4], which constrains deployment in water-scarce regions. The concept of seawater electrolysis (SWE), using direct ocean water [5] or with minimal pretreatment [6], promises to unlock a nearly unlimited and globally distributed water resource (~97% of Earth's water) for hydrogen production, which aligns well with the requirement of global availability.

Nonetheless, the challenges of SWE remain significant [7–10]. The high chloride concentration of seawater leads to competing chlorine evolution reactions (ClER) at the anode [11–13], which reduce O_2 Faradaic efficiency and accelerate corrosion and electrode degradation [14]. Thermodynamically, Oxygen Evolution Reaction (OER) is more favorable than ClER (see Supporting **Information - Reactions**), suggesting that the use of seawater (SW) should not pose intrinsic limitations. However, OER requires four electrons, whereas ClER involves only two, leading to a kinetic disadvantage and an increasing contribution of ClER to higher current densities [15,16]. Meanwhile, at the

* Corresponding author.
E-mail address: daniele.sassone@iit.it (D. Sassone).

https://doi.org/10.1016/j.jpowsour.2026.240833
Received 27 March 2026; Received in revised form 29 May 2026; Accepted 24 June 2026
Available online 30 June 2026
0378-7753/© 2026 The Authors. Published by Elsevier B.V. This is an open access article under the CC BY license (http://creativecommons.org/licenses/by/4.0/).

cathode, Hydrogen Evolution Reaction (HER) drives local pH up by OH^- formation, which triggers precipitation of $Mg(OH)_2$, $Ca(OH)_2$, or carbonate salts; these deposits block active catalytic sites, increase overpotential, and undermine long-term stability [17].

The most employed strategy in the literature to address these two issues is the alkalinization of SW, whereby NaOH or KOH is added to increase the pH to highly alkaline values (≈14) [18,19]. Under strongly alkaline conditions, the thermodynamic gap between OER and ClER is significantly widened. This shift allows OER to overcome the intrinsic kinetic advantage of ClER, thereby effectively suppressing chlorine evolution even at high current densities. At the same time, the elevated pH induces the precipitation of insoluble hydroxides prior to entering the electrolyzer, thus mitigating related operational issues. While this strategy is effective in suppressing ClER, it introduces a fundamental trade-off between operational stability and process relevance, as it alters the original chemical complexity of seawater and makes it more closely resemble an Anion Exchange Membrane electrolyzer operating with lower-purity water. A more sophisticated attempt to directly exploit SW is represented by the so-called half-seawater electrolyzers (half-SWE) configuration. Here, SW is only supplied to the cathode, while alkaline solutions, either pure or derived from the previous, are used at the anode. Although this configuration cannot be considered a full-seawater electrolyzer (full-SWE), it still represents a partial effort toward utilizing a more sustainable electrolyte.

In this work, we have classified four different types of "SW" employed in the state-of-the-art publications on SWE: (i) *natural seawater* (NSW), i.e. untreated or simply filtered water collected directly from the ocean, including Mg/Ca^{2+} cations, (ii) *synthetic seawater* (SSW), i.e. a 0.5 M NaCl solution which represents only the main ionic component of SW; and (iii) and (iv) corresponding to the alkalized versions of (i) and (ii) electrolytes. In Table 1 we have collected all the published literature about the SWE reporting the catalysts, catholyte, anolyte and membrane exploited, together with some information about the stability tests.

From Tables 1 and it is evident that very few studies use NSW in its original form [22–24], with most employing it only after alkalinization [21,26–30]. More importantly, when considering publications on half-SWE systems, SSW emerges as the sole catholyte reported in the literature. This represents a critical limitation, as the use of NSW in half-SWE would lead to significant failure at the cathode. Accordingly, this study aims to address this gap in existing literature by providing new insights into the topic.

In this work, we experimentally demonstrated that the use of NSW in half-SWE systems leads to an uncontrolled back-diffusion of OH^- ions from the anode to the cathode, resulting in hydroxide precipitation on the cathode and, consequently, cathodic failure. We investigate and quantify how all studied ion-exchange membranes exhibit significant deviations from ideal permselective behavior commonly assumed in the literature. Rather than acting as perfect separators that enable exclusively migrative ion transport, they also permit diffusive transport mechanisms [16,31–34], which can significantly affect species crossover and overall device performance, particularly in asymmetric configuration [35,36]. In detail, we demonstrate:

(i) the occurrence of uncontrolled diffusive phenomena even in the absence of an applied potential, by monitoring the system under Open Circuit Potential (OCP) conditions in a half-SWE with an alkaline anolyte;
(ii) the deviation under applied potential by performing OER and HER;
(iii) the quantification of OH^- migrative flux in a half-SWE with a neutral pH anolyte containing a ferrocyanide solution, thereby coupling the HER with a purely electron-transfer oxidation, avoiding the formation of additional parasitic ionic species.

In all cases, all experiments were conducted and replicated analyzing the difference among: (a) cation-exchange, anion-exchange, and bipolar membranes (CEM, AEM, BPM); (b) the role of membrane thickness; (c) the electrode preparation technique, i.e. Catalyst Coating Membrane (CCM) or Substrate (CCS) and (d) the current density applied. A quantitative understanding of ion permeability and its impact on local chemistry is essential to assess the validity of direct SWE claims. However, these aspects have not yet been systematically addressed and can provide beneficial contributions across a broad range of applications beyond SWE.

2. Experimental

2.1. Materials

Iron(III) chloride hexahydrate ($FeCl_3 \bullet 6H_2O$, ≥98.0%), potassium chloride (KCl, ≥99.0%), sodium chloride (NaCl, ≥99.5%), sodium hydroxide (NaOH, pellets 98.0-100.5%), 2-propanol (C_3H_8O, ≥99.8%), acetone (C_3H_6O, ≥99.5%), ethanol (C_2H_6O, 96%), sulfuric acid (H_2SO_4, 95.0-97.0%), hydrochloric acid (HCl, 37%) were purchased from Sigma-Aldrich. Nickel(II) chloride ($NiCl_2 \bullet 6H_2O$, 98%) was purchased from Alfa Aesar. Sodium ferrocyanide decahydrate ($Na_4Fe(CN)_6 \bullet 10H_2O$, ≥98.5%) was purchased from Thermo Fisher. A commercial sea salts mix (Instant Ocean) was used for SW preparation with high reliability, closely matching the composition [37] of natural seawater. Deionized (DI) water (resistivity: 18.3MΩ cm) was used for the preparation of all aqueous solutions, while tap water only for the SW one.

Platinum on Vulcan XC-72R (20 wt% Pt/C, Fuel Cell Store) and $NiFe_2O_4$ (see below) were used as benchmark catalysts for cathode and

Table 1
State-of-the-art selection of two-electrode electrolyzers, ordered by year of publication. Identical catalysts for anode and cathode are indicated by the entry "*both*." Stability information refers to lifetime, applied current density, and operating temperature. LDH: Layered Double Hydroxides. NFs: Nanoporous Films. NWs: Nanowires. NSW: Natural Seawater. SSW: Synthetic Seawater. n.r.: Not Reported.

Year	Cathode||Anode Catalysts	Catholyte	Anolyte	Membrane	Stability information	Ref.
2019	Ni-NiO-Cr_2O_3 || NiFe/NiS_x-Ni foam	1 M KOH + SSW	1 M KOH + SSW	None	1000 h, 400 mA cm^{-2}, 23°C	[20]
2020	Pt/C || NiFe-LDH	SSW	0.5 M KOH	AEM	100 h, 200 mA cm^{-2}, 50°C	[19]
2020	NiMoN || S-(Ni,Fe)OOH	1 M KOH + NSW	1 M KOH + NSW	None	100 h, 500 mA cm^{-2}, n.r.	[21]
2021	Fe,P-$NiSe_2$ NFs (*both*)	NSW	NSW	AEM	200 h, 800 mA cm^{-2}, 50°C	[22]
2023	Pt_{SA}-amorphous NiFeP NWs || amorphous NiFeP NWs	SSW	4 M NaOH	CEM	100 h, 100 mA cm^{-2}, 25°C	[18]
2023	Pt black || IrO_2	NSW	NSW	BPM	400 h, 250 mA cm^{-2}, n.r.	[23]
2023	Cr_2O_3–CoO_x (*both*)	NSW	NSW	CEM	100 h, 500 mA cm^{-2}, 23°C	[24]
2023	CoP/C on Ni@Ni_xP_y || NiFe-LDH on Ni@Ni_xS_y	dry N_2	1 M KOH + NSW	AEM	100 h, 400 mA cm^{-2}, 60°C	[15]
2024	Pt/C || S-$NiFeSe_2$	1 M KOH + NSW	1 M KOH + NSW	None	100 h, 10 mA cm^{-2}, n.r.	[25]
2024	Pt/C || CrO_4^{2-}-NiFe LDH/Cr_2O_3	1 M KOH + NSW	1 M KOH + NSW	AEM	200 h, 500 mA cm^{-2}, 23°C	[26]
2025	F-doped NMO || NiFe-LDH-PO_4^{3-}	1 M KOH + NSW	1 M KOH + NSW	Diaphragm	500 h, 500 mA cm^{-2}, 60°C	[27]
2025	P-NiFeMo || Raney nickel	6 M KOH + NSW	6 M KOH + NSW	Diaphragm	500 h, 500 mA cm^{-2}, 80°C	[28]
2025	Ni foam || NiFeZn-LDH	20 wt% NaOH + NSW	20 wt% NaOH + NSW	Diaphragm	500 h, 3 A cm^{-2}, n.r.	[29]
2025	Mo-O_FeP || S-(Ni,Fe)OOH	1 M KOH + NSW	1 M KOH + NSW	AEM	100 h, 100 mA cm^{-2}, 70°C	[30]

anode respectively, as Pt-based and Ni-based materials are the traditional catalysts used for HER [38,39] and OER [40,41] in alkaline and AEM-based systems. The substrates used were commercial carbon fiber paper (CFP) (Sigracet 28AA, Fuel Cell Store), and a nickel foam (NF) (purity 99.5%, thickness 0.9 mm, GoodFellow). As binder, Sustainion XA-9 5 wt% (Dioxide Materials) was used. As membranes, the AEMs selected were Fumasep FAB-PK-130 (FAB, from Fuel Cell Store), PiperION (PIPxxu, from Fuel Cell Store, where xx refers to the thickness: 40, 60, and 80 μm), and Sustainion X37-50 Grade RT (SUST, from Dioxide Materials), which are all commercial AEMs commonly used in alkaline electrolysis [42] and CO_2 electroreduction studies [43,44]. As references for PEM and BPM, Nafion N117 (NAF, from Ion Power) and Fumasep FBM-PK (FBM, from Fuel Cell Store) were employed, respectively, both of which are established materials in electrochemical and electrodialysis applications [45,46].

2.2. $NiFe_2O_4$ synthesis

$NiFe_2O_4$ was synthesized through co-precipitation [47] and annealing [48] methods. The target weight was set to 2 g. 8.5 mmol of $NiCl_2 \bullet 6H_2O$ and 17 mmol of $FeCl_3 \bullet 6H_2O$ were stirred together in 50 mL of DI water for 15 min. Controlled drops of 0.5 M NaOH were added while stirring until brown precipitates appeared and the measured pH was around 9-10. After that, the solution was stirred and heated at 70°C for 1 h. The solution was centrifugated at 4000 rpm for 10 min, to obtain the resulting compound. Then, it was rinsed in DI water and centrifugated four times to remove any contamination. The final compound was dried overnight at 60°C first, to remove the excess water, ground in a mortar to increase surface area and then annealed at 600°C for 3 h, both made in an air oven (Nabertherm B410). Before any use, it was ground again until fine powder was obtained. The final mass was 1.91 g, with a yield of 95.5%.

2.3. XRD

X-ray Diffraction (XRD) patterns were acquired in a Bragg-Brentano geometry with a Panalytical Xpert Pro diffrattometer (Cu-Kα radiation, voltage 40 kV, current 40 mA) equipped with an X' Celerator 1D detector in a 2θ range of 10–80° with 0.026° step size. The resulting analysis is shown in Fig. S1.

2.4. Electrode preparation

Catalysts were deposited through spay-coating (Nadetech Spray Coater, Ultrasonic Nozzle) onto the substrate or membrane, as the spatial disposition of the catalyst layer leads to distinct behaviours [49] and performance characteristics under operating conditions [50]. The ink contained catalyst, binder and solvent, chosen according to the different substrates and membranes (see Supporting **Information – Spray Coater** and Table S1), in which the mass loading of catalysts was fixed to 0.5 $mg_{Pt}\ cm^{-2}$ for Pt/C and 5 $mg\ cm^{-2}$ for $NiFe_2O_4$, regardless of the configuration, and the binder content to 20 wt% of catalyst. Before any use, the ink was sonicated for 30 min in a water bath, with no active heating. The heating plate's temperature under the target (substrate or membrane) was set in order to favor solvent evaporation. The deposition efficiency was evaluated to 50% in all the cases. Two separated tubes for ink injection were used to avoid catalyst cross-contamination. The active area was 2 cm^2.

2.5. Cell assembly

The Membrane Electrode Assembly (MEA) was assembled (reading order: from cathode to anode) using the CFP, the membrane under evaluation, and the NF. The CFP and NF layers served a dual function, acting both as current collectors and gas diffusion layers (GDLs). The presence and placement of catalytic layers within the MEA were adjusted according to the type of experiment performed, as detailed in the following subsections. The bipolar plates of the cell were custom-made from 904L stainless steel and served a dual purpose, acting as polarizable plates and enabling electrolyte circulation through a serpentine flow path. The electrolyzer was assembled by placing two Teflon gaskets (from Fuel Cell Store) between the bipolar plates and the MEA, with thicknesses of 127 μm (0.005″) and 508 μm (0.02") for the cathodic and anodic sides, respectively. The gasket selection accounted for the compression properties of the two substrates used. The cell was tightened using a torque wrench set to 2 Nm.

2.6. Electrolyzer testing

The two electrolytes were circulated in loop, using a peristaltic dispensing pump (Drifton LP-WT600-1F) synchronously at a flow rate of 100 mL min^{-1}. The tubing dimensions and lengths were custom-built to ensure symmetrical inlet and outlet paths for both liquids. The experiments were conducted at ambient temperature (23 ± 1°C) for both the cell and the electrolytes. The pH was measured using a benchtop pH meter (Fisherbrand Accumet AB150), calibrated by the three-point method (4.0 - 7.0 - 10.0) with standard buffer solutions purchased from Hanna Instruments at room temperature. The instrument was connected to its dedicated software with a baud rate set to 9600 Bd and a resolution of 3 digits (±0.001). Data acquisition was configured to record every 10 s and initiated once the electrolytes reached the MEA and the initial value had stabilized. The cell was connected to a potentiostat (Metrohm Multi Autolab/M204) in device mode. Stability and efficiency tests were carried out by chrono-potentiometry (CP), with data acquisition every 5 s. A delay of 5 s was introduced after current application to exclude the initial transient spike. Three independent experiments were conducted for each test type.

Fig. 1 presents a generalized schematic of the experimental setup developed for the asymmetric-feed configuration, employing the equipment described above. In this design, SW, after undergoing a filtration process to remove any biologic content (cells, algae, microorganisms) was consistently used as catholyte, while the remaining cell parameters and the anolyte were systematically varied to assess their impact on operation. Depending on the experiments, either 0.5 M NaOH or 0.1 M $Na_4Fe(CN)_6$ were used as anolytes, as detailed in the following sections.

3. Results and discussion

3.1. No-bias test: spontaneous ionic diffusion

For the first set of experiments, an alkaline anolyte (0.5 M NaOH) was used, and no external potential was applied. This preliminary analysis presents as an initial assessment of diffusion under a concentration gradient, which is a critical factor in a system where the separation of electrolytes across a high OH^- concentration gap is governed solely by the ionic membrane. The test was carried out first with AEMs and without catalysts, since at zero potential they are not involved and provide no additional contribution. The bulk pH (hereafter, always reported simply as pH) of the catholyte was monitored continuously, along with the OCP.

As shown in Fig. 2a, when the two solutions are in contact through three different AEMs, a diffusion of OH^- occurs, as can be observed from the increase in pH of the seawater. Therefore, an opposite diffusion of Cl^- ions from the cathode to the anode occurs. Given that the anolyte is sufficiently alkaline, the presence of these Cl^- ions does not contribute to any failure of the half-SWE; therefore, their quantification is neglected in this study. Diffusion occurs locally within the MEA structure and, over time, leads to the basification of the seawater until the theoretical precipitation level of magnesium hydroxide is reached. It is also observed that, after reaching this level, it tends to decrease in the following minutes. This phenomenon is attributable to the consumption

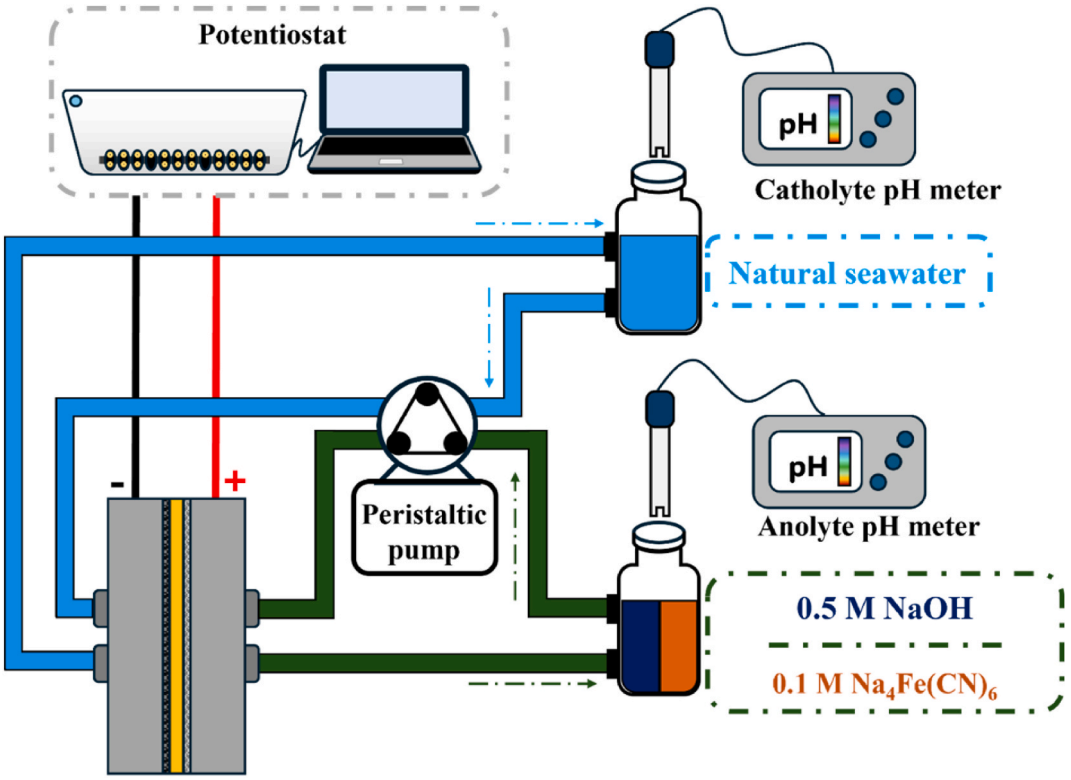

Fig. 1. Schematic of the asymmetric feed electrolyzer setup.

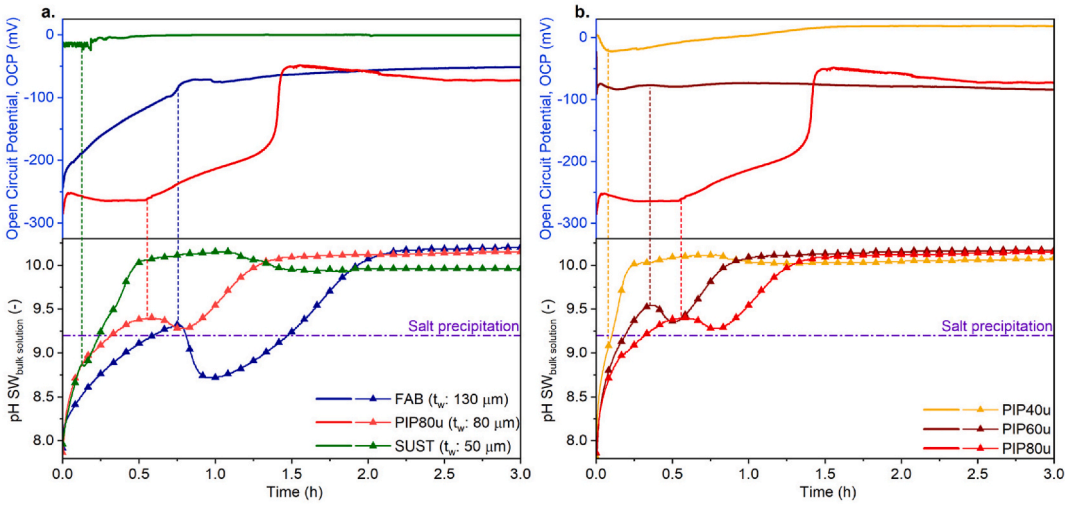

Fig. 2. **(a.)** Measurements of OCP and SW pH (bulk solution) in the no bias test with several commercial AEMs. **(b.)** Variation of OCP and the pH increment using the same membrane in different thicknesses.

of OH^-, diffusing from the anode, by Mg and Ca cations that form insoluble hydroxides. When most of these cations have completely precipitated as insoluble salts, the pH tends to rise again, stabilizing at a value around 10.2-10.3. In this phase, the gradient is not strong enough to register a further fast diffusion of OH^-, reaching a sort of equilibrium point. A distinct inflection point emerges in both pH(t) and OCP(t) curves (where t is the elapsed time), signaling saturation of SW and acceleration of catholyte basification, which is accompanied by the onset of insoluble salt precipitation. The observed transient decrease in pH during the precipitation phase, rather than a monotonic increase or a perfectly flat plateau, is a documented phenomenon in the crystallization kinetics of alkaline earth hydroxides, particularly magnesium hydroxide. This behavior can be attributed to the transition from a supersaturated metastable state to rapid primary nucleation [51].

From the comparison of different types of AEMs (having different ionomers and polymer chain conformation), the basification and resulting precipitation occurs over different time. The membrane thickness plays an important role, highlighted by Fig. 2b, where comparing different thickness of membranes with the same ionomer, causes different velocities in the basification and consequent pH inflection. For extremely thin membranes, such as PIP40u or SUST (Fig. S2a), the inflection in the pH profile is practically imperceptible, suggesting that, in addition to back-diffusion, a less efficient separation between the two solutions may also be taking place. Moreover, as the

diffusive flux is governed by the concentration gradient, mass transport is enhanced at shorter inter-electrode distances. Consequently, thinner membranes exhibit steeper hydroxide ion concentration gradients and higher diffusive fluxes, whereas thicker membranes lead to reduced gradients and lower fluxes. The diffusion flux of hydroxide ions through the membranes shown in Fig. 2b was estimated using the Nernst-Planck equation [52–54] and found to be on the order of 10^{-7} mol s^{-1} (additional details are provided in Table S2). Accordingly, the concentration required for salt precipitation at the membrane/electrode interface, where supersaturation conditions are expected to develop earlier, is expected to be reached after approximately 60, 90, and 120 s for PIP40u, PIP60u, and PIP80u, respectively. These times are in reasonable agreement with the experimental observations, although the experimentally measured pH corresponds to the bulk electrolyte reservoir, where salt precipitation is detected after longer times.

It is possible to visually detect hydroxide precipitation dispersed in the catholyte tank and after disassembling the cell (Fig. S3), both in the CFP and the serpentine path of the bipolar plate. Given that the concentration gradient is sufficiently steep to enable rapid diffusion of species across the membrane, we investigated whether like-charge repulsion constitutes a strong enough driving force to inhibit this diffusion. To study this aspect, a cation-exchange membrane, NAF, and a bipolar membrane, FBM, were also tested (Fig. S2b) for the same no-bias test. Both the NAF and the FBM tests showed the OH^- diffusion, resulting in the increase of catholyte pH, although with a slower rate than in the anion-exchange case; confirming the repulsion between charges of the same sign (OH^- with the SO_3^- from CEMs) is a force that opposes diffusion, strong enough to slow it down, but not enough to preventing it. At the same time scale, the no-bias test registers the lowest pH (i.e. slowest diffusion) for the FBM, as the OH^- have to pass through many layers, however, upon extending the test duration, as exemplified by the FBM case (Fig. S4), a shift in the inflection point is observed. This behaviour can be attributed to the localized increase in OH^- concentration predominantly taking place at the GDL-membrane interface, at the expense of the reservoir. To further elucidate this aspect, it would be necessary to measure the pH not in the bulk solution but directly at the membrane-electrode interfaces, which would be subject of future study. It should be noted that, within this treatment, Donnan exclusion, the fixed charge density of the membrane, and hydrated ion radii have not been considered. As such, the analysis relies on a simplified framework.

In conclusion, the use of an alkaline solution at the anode to promote OER over ClER leads to detrimental effects at the cathode when NSW is employed in the half-SWE. Since OH^- diffusion occurs from the anode to the cathode due to a concentration gradient, it is important to investigate how an external applied potential may counteract these driving forces. In fact, during water splitting, catholyte experiences an increase in pH due to OH^- generation, while anolyte undergoes acidification due to H^+ production. Under half-SWE operating conditions, these effects may modulate the diffusion driving forces between the two electrodes, that interact with the migration arising from the electrolysis. It should be noted that the interpretation of the time at which precipitation occurs is inherently qualitative, as the measurement is performed in the bulk solution rather than at the electrode interface.

3.2. Chrono-potentiometry test: ion migration and diffusion

With the same configuration of the previous section (NaOH and SW as anolyte and catholyte, respectively), we tested the half-SWE under operating conditions by applying a fixed current density of 100 mA cm^{-2} through CP, thereby increasing the complexity of the experimental setup by introducing ion migration driven by the applied electric field. We also investigated the effect of different catalyst deposition techniques, CCS/CCM, on the MEA performances, by utilizing only configuration in which both the anode and cathode exploit the same deposition technique.

The results obtained for the CCS configuration for all the investigated membranes are shown in Fig. 3a and Fig. S5. Applying an external potential required to reach 100 mA cm^{-2}, does not prevent the SW's basification, but rather postpone the time in which insoluble salts precipitation occurs. Compared to the no-bias case, the inflection point in the pH-versus-time curve is shifted to longer times, and the time coordinate of the maximum is reported in Fig. 3b. Among the membranes, PIP80u exhibits only a slight increase in this characteristic time, whereas SUST shows a pronounced improvement. For FAB, the pH does not reach the steady-state value within the 3 h experimental window because the growth rate after the inflection point is lower than for the other two membranes; it is therefore inferred that, by extending the CP working time, the stable pH is reached the same (Fig. S6). Under no-bias, the pH gradient across the electrochemical cell drives OH^- diffusion from the bulk electrolyte toward the anode, while upon application of bias, local pH at the anode decreases below bulk values due to water oxidation and OH^- consumption, while the cathode becomes more alkaline. Consequently, the overall ΔpH diminishes, reducing the chemical driving force for OH^- ion diffusion and potentially enhancing membrane performance by mitigating concentration polarization [55–58].

The migration flux of hydroxide ions was calculated for the membranes shown in Fig. 3a (see Table S3) and compared with the corresponding diffusive fluxes (Table S4). The calculations indicate that migration contributes more significantly to mass transport than diffusion, although both mechanisms are of the same order of magnitude. This behavior is attributed to the high applied bias, which promotes ion migration across the membrane. However, the applied bias also induces the in-situ generation of OH^- at the cathode during HER, with an estimated production rate on the order of 10^{-6} mol s^{-1}. This value slightly exceeds the calculated migration flux, so migration alone is not sufficient to efficiently remove the hydroxide species generated at the cathode. The resulting local OH^- accumulation, further enhanced by back-diffusion phenomena, is expected to promote salt precipitation and consequent cell degradation, likely explaining the experimental observations.

A further comparison is reported in Fig. 3c and d comparing the changes in SW pH and cell voltage using the same membrane but comparing the CCS and CCM preparation. The low mechanical stability of SUST did not allow to deposit the catalysts on the membrane to achieve a CCM. For FAB, the largest differences are observed, as changing from CCS to CCM deposition resulted in a deterioration of performance; specifically, the time to onset of precipitation is shorter for CCM, consistent with the faster pH increase measured in the catholyte. With respect to cell potential, an increase at the inflection point is evident for the CCS configuration, whereas no comparable change is observed for CCM. Due to the shorter contact distances and reduced interfacial resistances lower ohmic losses, CCM exhibits a lower cell potential than CCS. However, the CCM-CCS potential differences observed for PIP80u stem from fabrication challenges rather than intrinsic limitations. Its pronounced thinness promotes rapid water evaporation, resulting in a rough surface that hinders uniform catalyst deposition in CCM, causing an unwanted internal resistance increase, whereas CCS benefits from deposition on a flat, dry substrate. This issue was not observed for FAB. When the same experiment is repeated keeping the same MEA but regenerating the electrolytes, the potentials of CCS and CCM converge. These variations are reported in Fig. S7. This behaviour is attributed to contamination of the cathode-side membrane-deposited catalyst with residual cations, which decreases the HER activity and consequently increases the cell potential. The corresponding potential shift is less evident in the CCS configuration because the cathode catalyst layer is replaced before each experiment to avoid the effects of accumulated insoluble salts in the carbon support, which would otherwise render the electrode unusable. These considerations regarding potential behaviour also apply to PIP80u. Regarding pH, no appreciable extension of the time required to observe the inflection point is detected; only differences in the rate of pH increase are observed after the onset of seawater basification. The CCM configuration provides

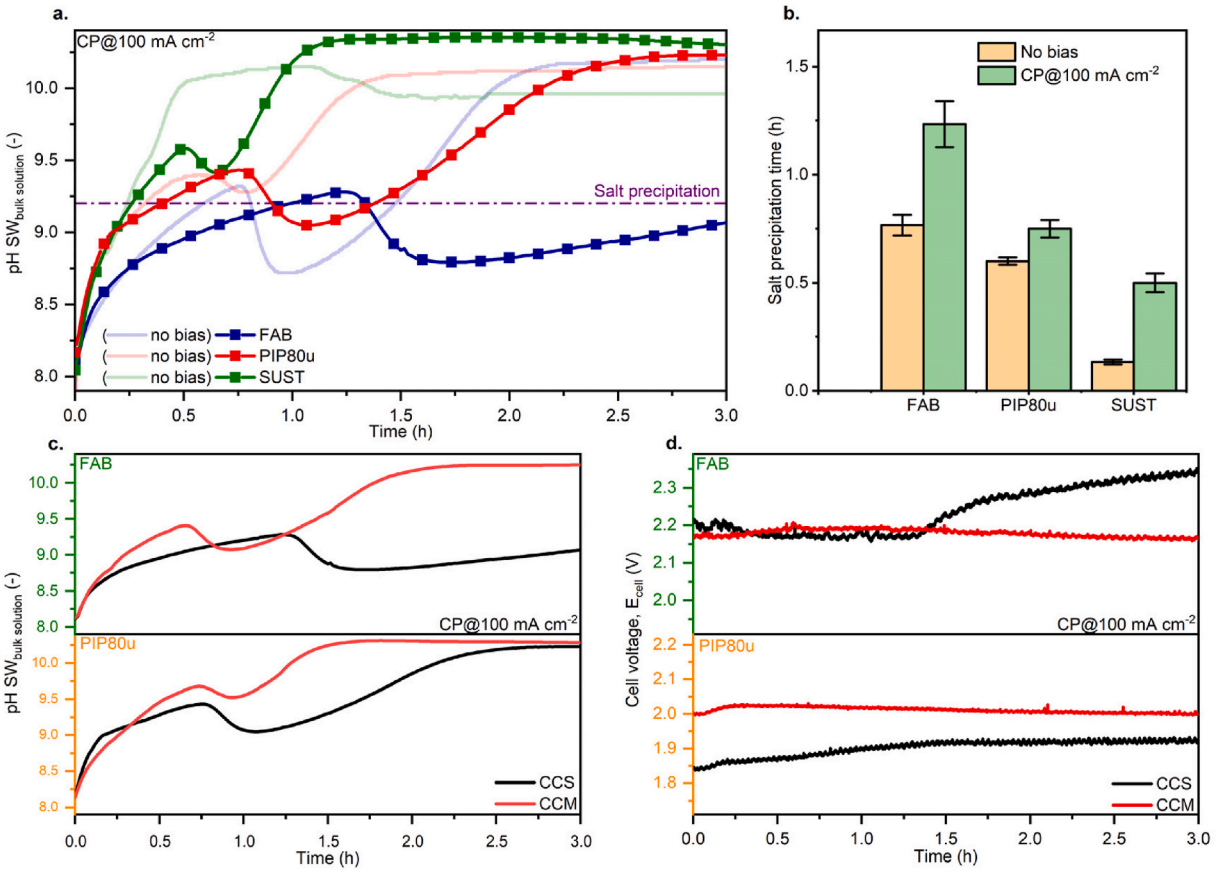

Fig. 3. **(a.)** Typical difference in SW pH trend between the no-bias and CP tests, where in the last the CCS placement was considered, with **(b.)** a highlight on the difference in time required for precipitation. Comparison in **(c.)** SW pH and **(d.)** voltage between the two main AEMs, FAB an PIP80u, with CCS and CCM placements.

enhanced interfacial contact between the catalyst layer and membrane surface compared to CCS [59,60], thereby facilitating greater hydroxide ion migration toward the anode and accelerated catholyte pH increase. Since OH^- back-diffusion is governed by the concentration gradient between electrolytes, basification occurs more rapidly in CCM.

To complete the analysis of the back-diffusion phenomenon, NAF and FBM were also evaluated. As predictable, for NAF (Fig. S8), seawater basification occurs significantly faster than for the AEMs, regardless of the catalyst placement: the characteristic inflection point in the pH trend is absent, and the pH exceeds the previously identified stability value of 10.2 within a few minutes, respect to the registered 3h without bias, with consequent accumulation of precipitates in the catholyte flow channels. When a CEM is employed, charge transport to close the electrical circuit is dominated by cation migration from the cathode to the anode. Consequently, OH^- ions accumulate to a greater extent on the cathode side compared to systems using an AEM, where partial OH^- transport toward the anode contributes to maintaining charge neutrality.

The FBM membrane (Fig. S9) represents a distinctive case. It was evaluated exclusively under CCS conditions for the same reasons discussed for the SUST sample, and at reduced current density (25 mA cm^{-2}) to preserve moderate electrochemical activity while limiting excessive cell voltages, due to larger ohmic resistance exhibited by this membrane. The evolution of pH in the SW compartment followed a trend comparable to that observed in the no-bias test; however, after approximately 3 h, a change in slope was detected, indicating the onset of hydroxide precipitation, which was later confirmed upon cell disassembly. The failure to reach the theoretical pH of 9.2 can be rationalized by considering the simultaneous reactions occurring within the MEA: at the cathode, the Pt catalyst promotes the HER, generating hydroxide ions that increase the local pH, while within the inner layer water splitting takes place, producing H^+ ions that permeate through the CEM layer of the bipolar membrane toward the cathode. The recombination of these ions at the GDL-CEM interface suggests a theoretically neutral local environment; nonetheless, the dominant cathodic activity favours local basification, not fully captured by the pH sensor but evidenced by the formation of salt precipitates. The rapid pH increase over time further supports the conclusion that the contribution of back-diffusion is secondary, in agreement with the behaviour previously observed for the NAF membrane.

In summary, these experiments indicate that, under an identical experimental setup and with the same electrolyte combination, the application of an electrical bias leads to distinctly different behaviors in OH^- transport. Apart from the CEM case, in which OH^- accumulation predictably worsens, systems employing AEMs show that the applied potential does not fully inhibit OH^- back-diffusion; rather, it partially counteracts it. This effect is presumably associated with the establishment of a reduced OH^- concentration gradient between the electrodes, thereby decreasing the driving force for back-diffusion. Comparison between CCS and CCM configurations showed that although CCM reduced cell resistance and initial potential due to improved catalyst-membrane contact, it led to a faster pH increase and earlier precipitation. These results highlight a trade-off between enhanced ionic transport in CCMs and increased susceptibility to catholyte basification, as well as the role of catalyst contamination. Further investigations employing complementary experimental approaches will therefore be required to elucidate the underlying mechanisms.

3.3. *Electron transfer test: hydroxide migration efficiency*

In the previous sections, we showed that using an alkaline anolyte to implement a half-SWE, aimed at mitigating the ClER, ultimately fails at

the cathode once a proper NSW is being used. This limitation motivates the shift toward full-SWE systems, in which SW is employed simultaneously as both anolyte and catholyte, thus eliminating an initial pH gradient between the two compartments; even if it would shift the challenge to the anodic side, related to OER/ClER competition. In a full-SWE configuration, AEMs and BPMs, operating under reverse bias, are expected to provide the most favorable contribution to ClER suppression at the anode and to mitigating salt precipitation at the cathode. In both cases, the underlying strategy is to drive the OH^- gradient generated at the cathode toward the anode, thereby preventing excessive alkalization of the catholyte while increasing the anodic pH to favor the OER over the ClER. An ideal AEM would selectively transport OH^- over the abundant Cl^- (and the other anions present in SW), whereas a reverse-biased BPM would optimally counteract the pH gradient imposed by the HER/OER through opposing H^+ and OH^- fluxes.

To assess the membrane capability to transport the ions relevant for full-SWE operation, a tailored half-SWE experiment was designed using a sodium ferrocyanide solution ($Na_4[Fe(CN)_6]$) as the anolyte instead of SW. Since the $Fe^{2+/3+}$ redox reaction involves only electron transfer (see Supporting **Information - Reactions**) and does not alter the anolyte pH, thus any variation can be ascribed solely to OH^- migration/diffusion across the membrane [61]. By comparing the initial and final anolyte pH, the amount of OH^- transported can be quantified relative to that produced at the cathode, enabling the determination of an OH^- migration rate for the AEMs under investigation. The ferrocyanide solution was selected respect to SW to prevent (i) the undesired ClER, (ii) the OH- production arising from OER, and (iii) OH^- diffusion for concentration gradient.

The efficiency of OH^- transport through the membrane was evaluated by monitoring the pH of the solution as a function of time and relating the initial value to the one measured at a given time. Being the sodium ferrocyanide a neutral pH solution, we can consider the pH variation occurring at the cathode solely to OH^- migration. From this relationship, the mole of OH^- that migrates from cathode to anode as a function of time can be determined according to the following equation:

$$n_{migrated\ OH^-}(t) = \left(10^{-pOH(t)} - 10^{-pOH(t_0)}\right) * V_{bulk}\ [\boldsymbol{mol}] \quad (1)$$

where $pOH(t)$ is the OH^- concentration measured by the pH meter at a specific time t, evaluated as $pOH = 14 - pH$, while $pOH(t_0)$ at the initial time, and V_{bulk} is the volume (in litres, L) considered for this experiment. It was assumed that all migrating ions originate from the HER reaction. From that, we can evaluate the amount of charge consumed to make them migrate, and since the ferrocyanide ions require only one electron to be oxidized, the calculation is the following one:

$$Q_{migration}(t) = n_{migrated\ OH^-}(t) * F\ [\boldsymbol{C}] \quad (2)$$

where F is the Faraday constant (96485.3365 C mol^{-1}). Knowing that current (density) is constant, and given the OH^- flux at a specific time, the total charge supplied to the cell and the charge associated with OH^- migration can be calculated, thereby allowing determination of the migration efficiency (η_{OH^-}), according to the following equation:

$$\eta_{OH^-}(t) = \frac{Q_{migration}(t)}{Q_{supply}(t)} * 100 = \frac{Q_{migration}(t)}{I * t} * 100\ [\%] \quad (3)$$

where I is the current applied. The necessity to define a migration efficiency arise from the fact that the charge balance between anode and cathode is partially maintained by Cl^- migration, with a smaller contribution from Na^+ one. Ideally, if our half-SWE could exploit only OH^- migration, the proper condition to pursuit HER and OER exploiting SW could be followed without occurring in any failure.

In a first analysis, the objective is to compare the ion migration capabilities as a function of AEM properties and the CCS/CCM realization with the catalyst. The testing methodology remains unchanged from the previous case, except for the use of a different anolyte, whose pH was additionally monitored, and the reduction of the applied current density to 50 mA cm^{-2}, as higher values could fasten the Fe^{2+}/Fe^{3+} oxidation reaction leading to total consumption of Fe^{2+} and thus to the occurrence of the water oxidation reaction with consequent OH^- consumption. The FAB and PIP80u membranes were tested, discarding the SUST option, to have also an overall overview of the catalysts placement.

As expected from earlier assumptions, the pH of the sodium ferrocyanide solution increases with a logarithmic trend (Fig. 4a); consequently, the OH^- concentration increases linearly, in agreement with the constant applied current. The difference in the rate of increase between the CCS and CCM configurations is nearly imperceptible in the case of PIP80u, whereas a slight difference (on a logarithmic scale) can be observed for the FAB membrane. This behaviour is consistent with what was previously observed for the asymmetric configuration and is further confirmed by the efficiency evaluation shown in Fig. 4c.

Although the overall efficiencies show comparable magnitudes, the CCS configuration generally exhibits higher hydroxide migration efficiencies but also greater variability between experiments. This effect is particularly evident for the FAB membrane, where the correlation among replicate measurements appears less robust compared PIP80u. Unlike the previously observed voltage stability, a progressive increase in cell potential was recorded during the experiment (Fig. 4b). This behaviour arises from the continuous recirculation and gradual consumption of the ferrocyanide solution, which leads to the dominance of OER and thus higher cell voltages. As the anolyte becomes increasingly alkaline, back-diffusion of hydroxide ions occurs again; therefore, an anodic reaction capable of generating H^+ species is required to buffer the excess alkalinity and limit OH^- migration. The pH of the catholyte (Fig. S10) was also monitored to assess the counterpart of OH^- ions that did not migrate through the membrane, confirming their accumulation on the cathodic side and thus providing complementary insight into the extent of back-diffusion suppression among the different configurations.

The preliminary conclusion of this experiment primarily focuses on the calculated efficiencies, which do not exceed 80% once a steady-state value is reached. This represents a major limitation in systems where efficient removal of OH^- ions from the cathode is required. The remaining fraction not contributing to ion migration can be attributed to the back-diffusion of hydroxide ions from the anode to the cathode, as the pH difference between the two electrolytes becomes sufficient to establish a concentration gradient, together with the transport of different ions inside the membrane (Cl^- and Na^+). An additional contributing factor is the local accumulation of these ions at the GDL-membrane interface, where limited migration under the applied electric field promotes SW basification, as confirmed by the catholyte pH measurements. The behaviour observed during the initial stages of testing can be explained by the membrane's working conditions: not all functional groups within the membrane were initially replaced by hydroxide ions, thus requiring a preliminary period for complete ion exchange to occur.

Following previous comparisons, attention was directed toward evaluating how the applied current density affects the OH^- migration process. Accordingly, the same experiment was performed at various current densities, 25, 50, 75, and 100 mA cm^{-2}, repeated three times to assess the response in terms of reproducibility (Figure S11a and Figure S12a). Peak efficiency values for both membranes under CCS and CCM configurations are shown in Fig. 5. Predictably, OH^- migration efficiency increases with current density, but only above 50 mA cm^{-2} and primarily in the CCM configuration. In contrast, an opposite trend is observed in CCS, where peak efficiency occurs at 75 mA cm^{-2}, as it may be ascribed to non-ideal zero-gap conditions of the MEA when catalysts are supported. Data correlation across tests is stronger for PIP80u due to its higher conductivity, while no clear dependence on current density was observed in terms of reproducibility.

At higher current densities, the oxidation of ferrocyanide ions proceeds more rapidly, until most of them are oxidized and the OER becomes predominant. In such conditions, hydroxide ions generated at the

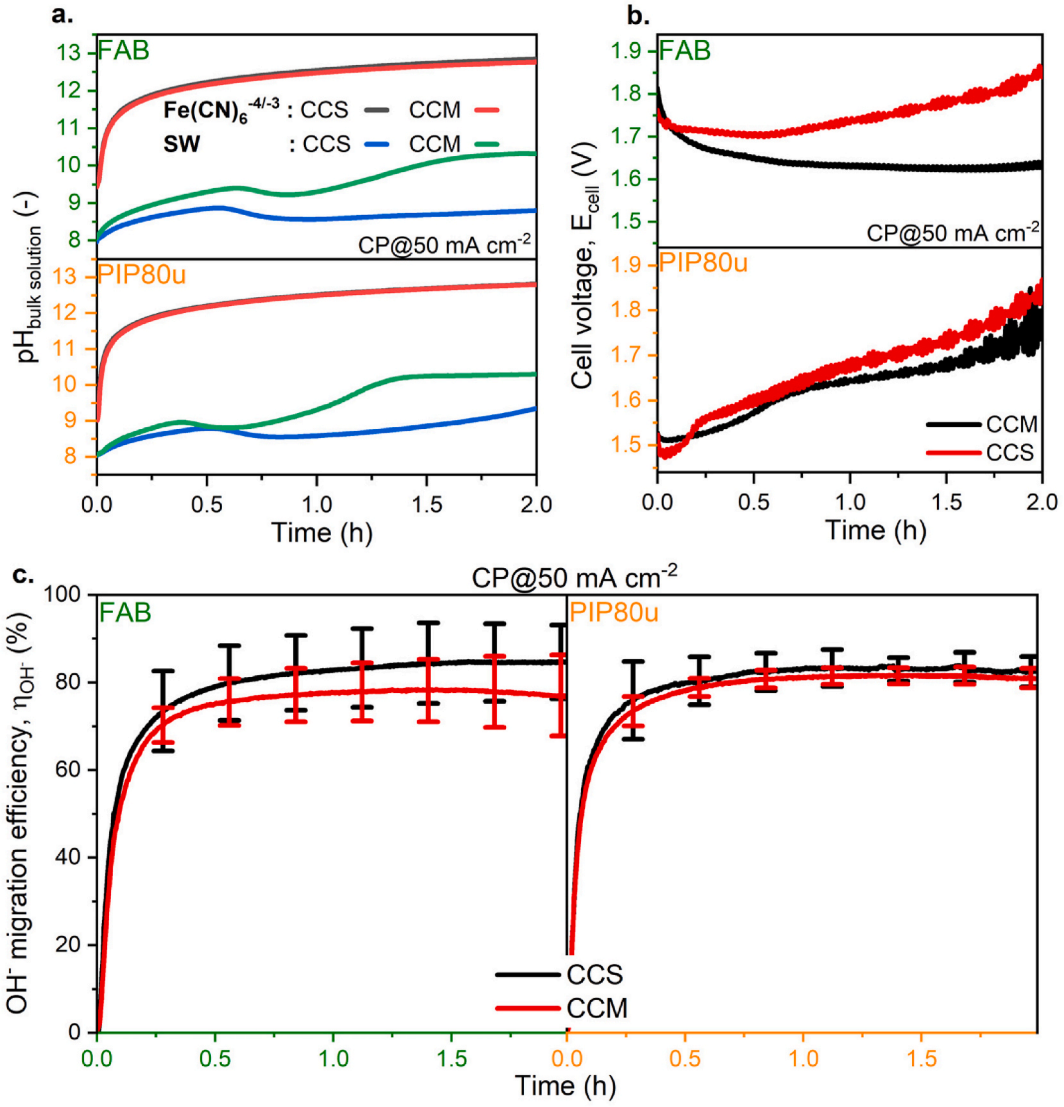

Fig. 4. Major information of the half-SWE coupled with ferrocyanide oxidation, tested with both FAB and PIP80u, and CCS and CCM placements. Typical trends of the **(a.)** pH of the electrolytes and **(b.)** cell voltage over time of the considered AEMs. **(c.)** Comparison of the migration efficiency over time.

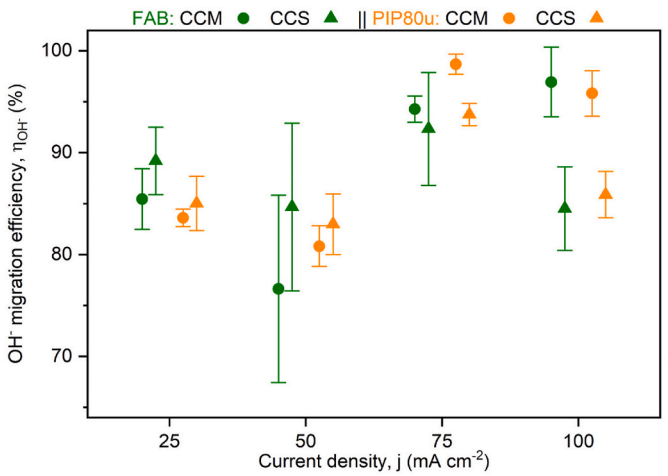

Fig. 5. Efficiencies (with correlations) of all the tested configurations in different current density for the SW-Ferrocyanide electrolyzer.

cathode are consumed at the anode, making migration efficiency estimation less reliable. This loss of information manifests as a decrease in efficiency after reaching its maximum and maintaining stability for a limited period. Supporting this interpretation, the cell voltage increases concurrently with the efficiency drop (Figure S11b and Figure S12b), reaching values comparable to those previously recorded for configurations with a basic anolyte. However, this trend is only partially reproducible in the CCS configuration, where voltage consistently increases over time, with varying intensity depending on current density. Furthermore, the efficiency peak is reached faster in CCS, followed by a progressive decline for the remainder of the experiment.

In summary, we confirmed that hydroxide migration efficiency remains a crucial factor for half-SWE. Concurrent pH monitoring of both electrolytes reveals hydroxide accumulation at the cathodic side due to limited migration and back-diffusion once alkalinity rises in the anolyte. Increasing current density enhances migration efficiency mainly in the CCM configuration, while in CCS the maximum efficiency occurs at 75 mA cm^{-2}, likely due to imperfect catalyst–membrane contact. Overall, the PIP80u membrane exhibits higher efficiency and better reproducibility compared to the FAB case. At high currents, rapid ferrocyanide oxidation leads to OER dominance and a corresponding efficiency decline accompanied by voltage growth, highlighting the interplay between membrane conductivity and ion transport dynamics.

4. Conclusions

In this work, it was highlighted how the use of improper terminology to define different types of SW often leads to poorly comparable results. By introducing a half-SWE setup, it was possible to investigate the crucial role of ion-exchange membranes and their integration with catalysts via CCS and CCM preparation methods. Regarding the membranes, it was demonstrated that they do not function as ideal charge separators; instead, they are subject to intrinsic and complex balances of chemical species transport driven by diffusion and migration principles. This was evidenced through experimental design featuring tests conducted both with and without applied bias. Thicker membranes delay but do not completely prevent these effects, confirming membrane functional group and thickness as primary bottlenecks over catalyst choice or configuration. Furthermore, this study suggests that half-SWEs based on alkaline anolytes may lack practical utility when utilizing natural SW. By developing a half-SWE that exploits an electron-transfer half-reaction, the potentials of different AEMs were screened to provide a framework for future research. Finally, PiperION was identified as the optimal compromise between migration efficiency and reproducibility. From these results, future research should prioritize experimental setups that maintain a non-critical pH differential across compartments, as it could be done by employing a BPM, to effectively promote both electrochemical reactions, a goal that necessitates direct investigation through full-SWE configurations.

Supporting information

The Supporting Information provides:

- Spray coater method and evaluation, XRD, electrochemical experiments with different membranes and setup

CRediT authorship contribution statement

Paolo Gardiol: Data curation, Formal analysis, Investigation, Writing – original draft. **Marco Etzi:** Conceptualization, Investigation, Supervision, Writing – review & editing. **Adriano Sacco:** Conceptualization, Funding acquisition, Writing – review & editing. **Cecilia Irene Gho:** Data curation, Formal analysis, Writing – original draft. **Daniele Sassone:** Conceptualization, Formal analysis, Project administration, Supervision, Validation, Writing – review & editing.

Declaration of competing interest

The authors declare that they have no known competing financial interests or personal relationships that could have appeared to influence the work reported in this paper.

Acknowledgments

The project was funded by the Project “Network 4 Energy Sustainable Transition—NEST”, Spoke 4: Clean Hydrogen and Final Use, Project code PE0000021, funded under the National Recovery and Resilience Plan (NRRP), Mission 4, Component 2, Investment 1.3— Call for tender No. 1561 of 11.10.2022 of Ministero dell'Università e della Ricerca (MUR); funded by the European Union—NextGenerationEU.

Appendix A. Supplementary data

Supplementary data to this article can be found online at https://doi.org/10.1016/j.jpowsour.2026.240833.

Data availability

Data will be made available on request.

References

[1] McKinsey & Company, Hydrogen for Net-Zero: a Critical Cost-Competitive Energy Vector, Hydrogen Council, 2021. https://hydrogencouncil.com/en/hydrogen-for-net-zero/.
[2] H. Ameli, D. Pudjianto, G. Strbac, N.P. Brandon, The impact of hydrogen on decarbonisation and resilience in integrated energy systems, Adv. Appl. Energy 17 (2025) 100200, https://doi.org/10.1016/j.adapen.2024.100200.
[3] M.B. Abdelghany, A. Shafiqurrahman, A. Al-Durra, M. Mohamed, J. Hu, A. Vaccaro, F. Gao, M.S. El Moursi, Hydrogen energy systems for decarbonizing smart cities and industrial applications: a review, Renew. Sustain. Energy Rev. 226 (2026) 116370, https://doi.org/10.1016/j.rser.2025.116370.
[4] H. Becker, J. Murawski, D.V. Shinde, I.E.L. Stephens, G. Hinds, G. Smith, Impact of impurities on water electrolysis: a review, Sustain. Energy Fuels 7 (7) (2023) 1565–1603, https://doi.org/10.1039/D2SE01517J.
[5] T. Liu, Z. Zhao, W. Tang, Y. Chen, C. Lan, L. Zhu, W. Jiang, Y. Wu, Y. Wang, Z. Yang, D. Yang, Q. Wang, L. Luo, T. Liu, H. Xie, In-Situ direct seawater electrolysis using floating platform in ocean with uncontrollable wave motion, Nat. Commun. 15 (1) (2024) 5305, https://doi.org/10.1038/s41467-024-49639-6.
[6] M. Khosravi, H. Thomas, L. Peeters, K. Holland, T. Hosseini, L. Carter, B. Bayatsarmadi, Y. Hou, Sustainable seawater electrolysis: evaluating environmental impacts and technological development opportunities, Sustain. Energy Fuels 9 (16) (2025) 4238–4261, https://doi.org/10.1039/D5SE00602C.
[7] L. Wu, Y. Xu, Q. Wang, X. Zou, Z. Pan, M.K.H. Leung, L. An, Direct seawater electrolysis for green hydrogen production: electrode designs, cell configurations, and system integrations, Energy Environ. Sci. 18 (10) (2025) 4596–4624, https://doi.org/10.1039/D5EE01093D.
[8] J.N. Bamba, A.T. Dumlao, R.M. Lazaro, D.D. Matienzo, J. Ocon, Green hydrogen from seawater electrolysis: recent developments and future perspectives, Curr. Opin. Electrochem. 48 (2024) 101592, https://doi.org/10.1016/j.coelec.2024.101592.
[9] B. Shetty, S. Puranam-Rajashekar, G.H. Aralikatti, P. Nagaraj, L.H. Kumar, P. N. Tengli, M.S. Thakur, Sridhar, M. Krishnappa, Seawater electrolysis: a critical review on fundamentals, recent progress, and future perspectives on sustainable hydrogen generation, Next Energy 9 (2025) 100407, https://doi.org/10.1016/j.nxener.2025.100407.
[10] Z. Feng, M. Zhang, C. Gu, A. Zhang, L. Wang, Seawater electrolysis: challenges, recent advances, and future perspectives, Adv. Sustain. Syst. 9 (1) (2025) 2400689, https://doi.org/10.1002/adsu.202400689.
[11] Hydrogen Production via Direct Seawater Electrolysis, Publications Office of the European Union, 2025, https://doi.org/10.2760/7173530.
[12] G. Bahuguna, F. Patolsky, Routes to avoiding chlorine evolution in seawater electrolysis: recent perspective and future directions, ACS Mater. Lett. 6 (8) (2024) 3202–3217, https://doi.org/10.1021/acsmaterialslett.4c00409.
[13] L.-J. Yang, H.-Y. Guan, S. Yuan, T. Sun, A.-N. Jiang, J.-J. Feng, Research progress of chlorine corrosion resistance in seawater electrolysis: materials and technologies, Chem. Eng. J. 503 (2025) 158458, https://doi.org/10.1016/j.cej.2024.158458.
[14] A. Goryachev, M. Etzi Coller Pascuzzi, F. Carlà, T. Weber, H. Over, E.J.M. Hensen, J.P. Hofmann, Electrochemical stability of RuO2(110)/Ru(0001) model electrodes in the oxygen and chlorine evolution reactions, Electrochim. Acta 336 (2020) 135713, https://doi.org/10.1016/j.electacta.2020.135713.
[15] M.L. Frisch, T.N. Thanh, A. Arinchtein, L. Hager, J. Schmidt, S. Brückner, J. Kerres, P. Strasser, Seawater electrolysis using All-PGM-Free catalysts and cell components in an asymmetric feed, ACS Energy Lett. 8 (5) (2023) 2387–2394, https://doi.org/10.1021/acsenergylett.3c00492.
[16] N. Du, C. Roy, R. Peach, M. Turnbull, S. Thiele, C. Bock, Anion-exchange membrane water electrolyzers, Chem. Rev. 122 (13) (2022) 11830–11895, https://doi.org/10.1021/acs.chemrev.1c00854.
[17] A. Badreldin, A. El Ghenymy, A.-R. Al-Zubi, A. Ashour, N. Hassan, A. Prakash, M. Kozusznik, D.V. Esposito, S.U.I. Solim, A. Abdel-Wahab, Stepwise strategies for overcoming limitations of membraneless electrolysis for direct seawater electrolysis, J. Power Sources 593 (2024) 233991, https://doi.org/10.1016/j.jpowsour.2023.233991.
[18] H. Shi, T. Wang, J. Liu, W. Chen, S. Li, J. Liang, S. Liu, X. Liu, Z. Cai, C. Wang, D. Su, Y. Huang, L. Elbaz, Q. Li, A sodium-ion-conducted asymmetric electrolyzer to lower the operation voltage for direct seawater electrolysis, Nat. Commun. 14 (1) (2023) 3934, https://doi.org/10.1038/s41467-023-39681-1.
[19] S. Dresp, T. Ngo Thanh, M. Klingenhof, S. Brückner, P. Hauke, P. Strasser, Efficient direct seawater electrolysers using selective alkaline NiFe-LDH as OER catalyst in asymmetric electrolyte feeds, Energy Environ. Sci. 13 (6) (2020) 1725–1729, https://doi.org/10.1039/D0EE01125H.
[20] Y. Kuang, M.J. Kenney, Y. Meng, W.-H. Hung, Y. Liu, J.E. Huang, R. Prasanna, P. Li, Y. Li, L. Wang, M.-C. Lin, M.D. McGehee, X. Sun, H. Dai, Solar-driven, highly sustained splitting of seawater into hydrogen and oxygen fuels, Proc. Natl. Acad. Sci. 116 (14) (2019) 6624–6629, https://doi.org/10.1073/pnas.1900556116.
[21] L. Yu, L. Wu, B. McElhenny, S. Song, D. Luo, F. Zhang, Y. Yu, S. Chen, Z. Ren, Ultrafast room-temperature synthesis of porous S-Doped Ni/Fe (oxy)Hydroxide electrodes for oxygen evolution catalysis in seawater splitting, Energy Environ. Sci. 13 (10) (2020) 3439–3446, https://doi.org/10.1039/D0EE00921K.
[22] J. Chang, G. Wang, Z. Yang, B. Li, Q. Wang, R. Kuliiev, N. Orlovskaya, M. Gu, Y. Du, G. Wang, Y. Yang, Dual-doping and synergism toward high-performance seawater electrolysis, Adv. Mater. 33 (33) (2021) 2101425, https://doi.org/10.1002/adma.202101425.
[23] D.H. Marin, J.T. Perryman, M.A. Hubert, G.A. Lindquist, L. Chen, A.M. Aleman, G. A. Kamat, V.A. Niemann, M.B. Stevens, Y.N. Regmi, S.W. Boettcher, A. C. Nielander, T.F. Jaramillo, Hydrogen production with seawater-resilient bipolar

membrane electrolyzers, Joule 7 (4) (2023) 765–781, https://doi.org/10.1016/j.joule.2023.03.005.
[24] J. Guo, Y. Zheng, Z. Hu, C. Zheng, J. Mao, K. Du, M. Jaroniec, S.-Z. Qiao, T. Ling, Direct seawater electrolysis by adjusting the local reaction environment of a catalyst, Nat. Energy 8 (3) (2023) 264–272, https://doi.org/10.1038/s41560-023-01195-x.
[25] X. Chen, Y. Yu, X. Han, H. Wang, Y. Hua, D. Wu, P. Deng, J. Xiao, X. Tian, J. Li, Introducing sulfur to nickel-iron selenide for high-efficiency alkaline seawater electrolysis, Sci. China Chem. 67 (8) (2024) 2747–2754, https://doi.org/10.1007/s11426-023-1965-y.
[26] Z. Cai, J. Liang, Z. Li, T. Yan, C. Yang, S. Sun, M. Yue, X. Liu, T. Xie, Y. Wang, T. Li, Y. Luo, D. Zheng, Q. Liu, J. Zhao, X. Sun, B. Tang, Stabilizing NiFe sites by high-dispersity of nanosized and anionic Cr species toward durable seawater oxidation, Nat. Commun. 15 (1) (2024) 6624, https://doi.org/10.1038/s41467-024-51130-1.
[27] D. Fu, X. Sun, F.-Y. Gao, Y. Zheng, S.-Z. Qiao, Fluorine-induced molybdate trap-and-buffer enables durable intermittent alkaline seawater electrolysis, Adv. Funct. Mater. (n/a) (2025) e26332, https://doi.org/10.1002/adfm.202526332 *n/a*.
[28] C. Li, X. Mao, M. Wang, L. Liu, J. Hu, X. Xu, Seawater electrolysis sustained via the permselective layer on catalysts, ACS Appl. Mater. Interfaces 17 (25) (2025) 36831–36839, https://doi.org/10.1021/acsami.5c07444.
[29] S. Li, W. Liu, X. Guo, B. Ding, A. Cao, Q. Sha, Z. Shen, Y. Yang, Y. Zhang, Y. Zhang, K. Wang, H. Xin, Y. Kuang, D. Zhou, X. Sun, Zincate ion enables M(II)-vacancy NiFe layered double hydroxide for stable seawater electrolysis at 3 A Cm−2, Small 21 (27) (2025) 2502994, https://doi.org/10.1002/smll.202502994.
[30] M. Li, C. Liu, Z. Teng, R. Zhang, X. Liu, J. Zhu, X. Liu, Z. Wu, Y. Chai, J. Chi, L. Wang, Manipulating interfacial water configuration via constructing asymmetric structure unit for hydrogen production in alkaline seawater, Adv. Funct. Mater. 35 (52) (2025) e14517, https://doi.org/10.1002/adfm.202514517.
[31] D. Li, A.R. Motz, C. Bae, C. Fujimoto, G. Yang, F.-Y. Zhang, K.E. Ayers, Y.S. Kim, Durability of anion exchange membrane water electrolyzers, Energy Environ. Sci. 14 (6) (2021) 3393–3419, https://doi.org/10.1039/D0EE04086J.
[32] N. Li, S.S. Araya, X. Cui, S.K. Kær, The effects of cationic impurities on the performance of proton exchange membrane water electrolyzer, J. Power Sources 473 (2020) 228617, https://doi.org/10.1016/j.jpowsour.2020.228617.
[33] G. Prats Vergel, H. Mu, N. Kolobov, J. Biemolt, D.A. Vermaas, T. Burdyny, Water dissociation efficiencies control the viability of reverse-bias bipolar membranes for CO2 electrolysis, Nat. Chem. Eng. 2 (11) (2025) 676–684, https://doi.org/10.1038/s44286-025-00306-7.
[34] Q. Zhang, Y. Hao, H. Chen, J. Li, Y. Zeng, J. Xiong, Y. Cheng, A. Ozden, A. Tricoli, F. Li, Toward energy-efficient alkaline water electrolysis: advances in mass transport optimization and electrolyzer design, Adv. Energy Mater. 16 (1) (2026) e04039, https://doi.org/10.1002/aenm.202504039.
[35] A.R. Fareza, H. Garg, D. Simondson, M.R. Rizk, T.D. Nguyen, H.-L. Du, D. R. MacFarlane, A.N. Simonov, Cell engineering can mitigate cathode scaling during water electrolysis in the presence of Mg2+, ACS Electrochem 1 (5) (2025) 763–773, https://doi.org/10.1021/acselectrochem.4c00189.
[36] H. Qazi, D. Chauhan, Y.-H. Ahn, Impurity impacts and mitigation strategies in alkaline seawater electrolysis, Int. J. Hydrogen Energy 99 (2025) 155–164, https://doi.org/10.1016/j.ijhydene.2024.12.196.
[37] B. Anes, C. Oliveira, R.J.B. da Silva, M.F. Camões, Characterization of seawaters by ion chromatography–comparison of ionic patterns and balances, Metrol. Sea 3-5 (2019).
[38] W. Ma, X. Zhang, W. Li, M. Jiao, L. Zhang, R. Ma, Z. Zhou, Advanced Pt-Based electrocatalysts for the hydrogen evolution reaction in alkaline medium, Nanoscale 15 (28) (2023) 11759–11776, https://doi.org/10.1039/D3NR01940C.
[39] X. Luo, P. Yuan, H. Xiao, S. Li, J. Luo, J. Li, W. Lai, Y. Chen, D. Li, Effects of intrinsic defects in Pt-Based carbon supports on alkaline hydrogen evolution reaction, ACS Appl. Mater. Interfaces 16 (20) (2024) 26044–26056, https://doi.org/10.1021/acsami.4c00690.
[40] R. Suzuki, K. Obata, Y. Sasaki, K. Adachi, K. Takanabe, Stability investigation on NiFeOx electrocatalysts for oxygen evolution during on and off cycles in harsh alkaline conditions, Chemelectrochem 12 (14) (2025) e202500081, https://doi.org/10.1002/celc.202500081.
[41] M. Etzi Coller Pascuzzi, A.J.W. Man, A. Goryachev, J.P. Hofmann, E.J.M. Hensen, Investigation of the stability of NiFe-(Oxy)Hydroxide anodes in alkaline water electrolysis under industrially relevant conditions, Catal. Sci. Technol. 10 (16) (2020) 5593–5601, https://doi.org/10.1039/D0CY01179G.
[42] A.J. Domańska, P.M. Skitał, Application of anion exchange membranes Fumasep FAA-3-PK-130 and PiperION as components of a laboratory electrolyzer for electrochemical hydrogen evolution, Adv. Sci. Technol. Res. J. 20 (1) (2026) 152–161, https://doi.org/10.12913/22998624/210473.
[43] Y. Zhao, H. Hua, S. Wei, J. Luo, Screening anion exchange membranes for CO2 electrolysis, ACS Appl. Mater. Interfaces 17 (40) (2025) 56164–56174, https://doi.org/10.1021/acsami.5c13225.
[44] B. Endrődi, A. Samu, E. Kecsenovity, T. Halmágyi, D. Sebők, C. Janáky, Operando cathode activation with alkali metal cations for high Current density operation of water-fed zero-gap carbon dioxide electrolysers, Nat. Energy 6 (4) (2021) 439–448, https://doi.org/10.1038/s41560-021-00813-w.
[45] J. Mališ, P. Mazúr, M. Paidar, T. Bystron, K. Bouzek, Nafion 117 stability under conditions of PEM water electrolysis at elevated temperature and pressure, Int. J. Hydrogen Energy 41 (4) (2016) 2177–2188, https://doi.org/10.1016/j.ijhydene.2015.11.102.
[46] B. Siritanaratkul, P.K. Sharma, E.H. Yu, A.J. Cowan, Improving the stability, selectivity, and cell voltage of a bipolar membrane zero-gap electrolyzer for low-loss CO2 reduction, Adv. Mater. Interfac. 10 (15) (2023) 2300203, https://doi.org/10.1002/admi.202300203.
[47] K. Maaz, S. Karim, A. Mumtaz, S.K. Hasanain, J. Liu, J.L. Duan, Synthesis and magnetic characterization of nickel ferrite nanoparticles prepared by Co-Precipitation route, J. Magn. Magn Mater. 321 (12) (2009) 1838–1842, https://doi.org/10.1016/j.jmmm.2008.11.098.
[48] Ž. Cvejić, E. Đurđić, G. Ivković Ivandekić, B. Bajac, P. Postolache, L. Mitoseriu, V. V. Srdić, S. Rakić, The effect of annealing on microstructure and cation distribution of NiFe2O4, J. Alloys Compd. 649 (2015) 1231–1238, https://doi.org/10.1016/j.jallcom.2015.07.238.
[49] S. Thanasilp, M. Hunsom, Effect of MEA fabrication techniques on the cell performance of Pt–Pd/C electrocatalyst for oxygen reduction in PEM fuel cell, Fuel 89 (12) (2010) 3847–3852, https://doi.org/10.1016/j.fuel.2010.07.008.
[50] L. Yang, S. Dong, T. Yang, J. Liu, S. Liu, K. Wang, E. Wang, H. Wang, K.-C. Chou, X. Hou, Membrane Electrode Assembly Design for High-Efficiency Anion Exchange Membrane Water Electrolysis, vol. 8, Research (Wash D C), 2025, p. 907, https://doi.org/10.34133/research.0907.
[51] C. Shaw, M.C. Ringham, B.R. Carter, M.D. Tyka, M.D. Eisaman, Using magnesium hydroxide for ocean alkalinity enhancement: elucidating the role of formation conditions on material properties and dissolution kinetics, Front. Clim. 7 (2025) 1616362, https://doi.org/10.3389/fclim.2025.1616362.
[52] A.J. Bard, L.R. Faulkner, H.S. White, Electrochemical Methods: Fundamentals and Applications, third ed., Wiley, Hoboken, NJ, USA Chichester, West Sussex, UK, 2022.
[53] F. Habibzadeh, P. Mardle, N. Zhao, H.D. Riley, D.A. Salvatore, C.P. Berlinguette, S. Holdcroft, Z. Shi, Ion exchange membranes in electrochemical CO2 reduction processes, Electrochem. Energy Rev. 6 (1) (2023) 26, https://doi.org/10.1007/s41918-023-00183-9.
[54] A. Alamdari, M.R. Rahimpour, N. Esfandiari, E. Nourafkan, Kinetics of magnesium hydroxide precipitation from sea bittern, Chem. Eng. Process. Process Intensif. 47 (2) (2008) 215–221, https://doi.org/10.1016/j.cep.2007.02.012.
[55] X.K. Lu, L.C. Seitz, Reactor operating parameters and their effects on the local reaction environment of CO(2) electroreduction, Chem. Soc. Rev. 54 (12) (2025) 6088–6121, https://doi.org/10.1039/D5CS00040H.
[56] H. Ooka, M.C. Figueiredo, M.T.M. Koper, Competition between hydrogen evolution and carbon dioxide reduction on copper electrodes in mildly acidic media, Langmuir 33 (37) (2017) 9307–9313, https://doi.org/10.1021/acs.langmuir.7b00696.
[57] X. Lu, C. Zhu, Z. Wu, J. Xuan, J.S. Francisco, H. Wang, In situ observation of the pH gradient near the gas diffusion electrode of CO2 reduction in alkaline electrolyte, J. Am. Chem. Soc. 142 (36) (2020) 15438–15444, https://doi.org/10.1021/jacs.0c06779.
[58] M.C.O. Monteiro, M.T.M. Koper, Measuring local pH in electrochemistry, Curr. Opin. Electrochem. 25 (2021) 100649, https://doi.org/10.1016/j.coelec.2020.100649.
[59] H. Park, S. Harris, P.A. Kohl, Anion exchange membrane water electrolysis using a catalyst-coated membrane cathode, ACS Electrochem 1 (11) (2025) 2495–2502, https://doi.org/10.1021/acselectrochem.5c00280.
[60] L. Titheridge, S.K. Sharma, A. Soisson, C. Roth, A.T. Marshall, Recent advances in understanding catalyst coated membranes vs catalyst coated substrates for AEM electrolysers, Curr. Opin. Electrochem. 49 (2025) 101607, https://doi.org/10.1016/j.coelec.2024.101607.
[61] J.E. Huang, F. Li, A. Ozden, A. Sedighian Rasouli, F.P. García de Arquer, S. Liu, S. Zhang, M. Luo, X. Wang, Y. Lum, Y. Xu, K. Bertens, R.K. Miao, C.-T. Dinh, D. Sinton, E.H. Sargent, CO2 electrolysis to multicarbon products in strong acid, Science 372 (6546) (2021) 1074–1078, https://doi.org/10.1126/science.abg6582.